Article

Synthesis of Manganese Ferrite/Graphene Oxide Magnetic Nanocomposite for Pollutants Removal from Water

Khadijah Mohammedsaleh M Katubi [1] , **Norah Salem Alsaiari** [1,*], **Fatimah Mohammed Alzahrani** [1,*] , **Saifeldin M. Siddeeg** [2,3] **and Mohamed A. Tahoon** [2,4]

1   Chemistry Department, College of Science, Princess Nourah bint Abdulrahman University, Riyadh 11671, Saudi Arabia; kmkatubi@pnu.edu.sa

2   Department of Chemistry, College of Science, King Khalid University, P.O. Box 9004, Abha 61413, Saudi Arabia; saif.siddeeg@gmail.com (S.M.S.); tahooon_87@yahoo.com (M.A.T.)

3   Chemistry and Nuclear Physics Institute, Atomic Energy Commission, P.O. Box 3001, Khartoum 11111, Sudan

4   Chemistry Department, Faculty of Science, Mansoura University, 35516 Mansoura, Egypt

*   Correspondence: nsalsaiari@pnu.edu.sa (N.S.A); fmalzahrani@pnu.edu.sa (F.M.A.)

Abstract: These days, environmental pollution, notably water pollution, has increasingly caused severe human health problems. The major water pollutants are heavy metals. $MnFe_2O_4/GO$ nanocomposite was prepared in the current work via in situ method and tested to remove lead ion Pb^{2+} and neutral red (NR) dye from water. The prepared nanocomposite was characterized using different techniques, including X-ray diffraction, transmission electron microscopy, Fourier transform infrared spectroscopy, scanning electron microscopy, X-ray photoelectron spectroscopy, Raman spectra, and vibrating sample magnetometer. The prepared nanocomposite showed high adsorption capacity toward Pb^{2+} and NR dye removal according to Langmuir fitting indicating the monolayer homogeneous adsorption of pollutants over the adsorbent surface and can be separated easily with an external magnet. The effect of different factors, including contact time, pH, initial concentration, and adsorbent dose on the adsorption, were also studied. The increased concentration of pollutants led to increased adsorption capacity from 63 to 625 mg/g for Pb^{2+} ions and from 20 to 90 mg/g for NR dye. The increased adsorbent dose led to increased removal efficiency from 39% to 98.8% and from 63% to 94% for Pb^{2+} and NR dye, respectively. The optimum pH for the adsorption of both pollutants was found to be 6.0. The reusability of $MnFe_2O_4/GO$ nanocomposite was studied for up to five cycles. The nanocomposite can keep its efficiency even after the studied cycles. So, the prepared magnetic nanocomposite is a promising material for water treatment.

Keywords: environment; water treatment; carbon-based nanomaterials; adsorption

1. Introduction

The environment and living organisms face serious health risks resulting from the continuous discharging of industrial effluents directly to the environment, such as cosmetics effluents, plastic, paper, textiles, leather, fertilizers, pesticides, fuel, and energy production, metallurgy, mining, and the discharged wastes that contain heavy metal ions [1–3]. The direct discarding of such harmful industrial pollutants without treatment is a significant concern [4]. Thus, many techniques are developed for the treatment of water/wastewater from toxic species, such as adsorption [5], co-precipitation [6], electrocoagulation [7], biochemical degradation [8], photocatalytic degradation [9], photo-degradation [10], oxidative degradation [11], and electrochemical degradations [12]. However, several reasons make the adsorption technique widely used for water treatment over other techniques, such as eliminating several types of toxins, high efficiency, less environmental effect, the ability to reuse adsorbents, and the ease of processing [13–15]. The examples of the most dangerous substances are heavy metal ions and organic dyes that have harmful environmental impacts.

Heavy metals can accumulate inside human and living organisms over a long-timescale as these metals are not metabolized inside organisms and humans [16]. In the current study, we focus on lead ions and neutral red dye. Lead ions are thrown away directly to the environment with automobiles industrial parts, paints, and batteries [17]. It is a very toxic metal and has a harmful effect on the central and peripheral nervous system [18]. Many dangerous effects include antisocial behaviors, nausea, loss of appetite, anemia, muscle paralysis, and abdominal pains. According to the World Health Organization (WHO), the lead ions limited concentration in blood should not exceed $0.1 \, \text{gm}^{-3}$ [19] that makes its removal from water/wastewater mandatory. Many efforts have been made for the removal of Pb^{2+} ions from water using different carbon-based materials such as the poly(acrylamide-co-itaconic acid)/multi-walled carbon nanotubes (MWCNTs) [20], mesoporous $NiO/ZnCl_2$-Rosa Canina-L seeds activated carbon nanocomposite [21], and magnetic Fe_3O_4/H_2SO_4-activated Myrtus Communis leaves carbon nanocomposite [22]. Dyes can consume soluble oxygen due to their deep color [23]. The degradation products of many dyes are poisonous and carcinogenic that can destroy marine organisms [24]. Cosmetic industries, food additives, textiles, paper industries, and leather are well-known dye sources [25]. Neutral red is a mono-cationic dye widely used in nuclear counterstaining in biological studies [26]. The direct release of these colored compounds leads to cancer, mutations, and carcinogenesis [27]. Hence, elimination of these pollutants from water/wastewater is essential to control the contamination of the environment. Carbon-based materials have been utilized to remove dyes from the water with high efficiency [28].

Nanomaterials [29–33] as adsorbents, especially magnetic ones such as ($MnFe_2O_4$, $NiFe_2O_4$, Fe_3O_4) are promising and widely used for water treatment in the last decade. However, these nanomaterials have many deficiencies, like agglomeration and instability [34]. Especially, nanoparticles of $MnFe_2O_4$ have many uses disadvantages such as ease of oxidation at low pH values, weak mechanical properties, agglomeration, and instability that makes its attachment to the substrate is essential to enhance their properties. The excellent dispersion and hydrophilic properties of graphene oxide resulted from various oxygen-containing functional groups, and high negative charge density on its surface and high specific surface area [35] enable it to be the ideal substrate to enhance magnetic $MnFe_2O_4$ NPs for water treatment applications. The attachment of graphene oxide and $MnFe_2O_4$ to form $MnFe_2O_4$/graphene oxide nanocomposite has enhanced properties over its counterparts such as high removal efficiency, magnetic separation, and reusability that can be perfect adsorbent for the elimination of neutral red dye and lead ions from wastewater. Various studies have been reported the combination of carbon-based materials and magnetic nanoparticles [36–38] for water treatment. Moreover, hierarchically porous reduced graphene oxide decorated with manganese ferrite (MrGO) was used to uptake methylene blue and malachite green dyes with high efficiency [39].

This study aimed to synthesize and characterize a novel nanocomposite of $MnFe_2O_4$/graphene oxide to absorb neutral red dye and lead ions from wastewater. The effect of different factors like contact time, adsorbent dosage, and pH on the adsorption process was investigated and discussed. The separation of the selected nanocomposite for reusability was determined. In a similar previous study, $MnFe_2O_4$/graphene oxide was synthesized for the removal of Pb^{2+}, As^{3+}, and As^{5+} from water [40]. As the synthesis method, conditions, and phase ratios in the composite affect the surface area of the adsorbent and, consequently, affect the nanocomposite's adsorption capacity. Therefore, the current study clarifies the suitable method and conditions of $MnFe_2O_4$/graphene oxide synthesis for more effective pollutants removal and determining the applicability of this nanocomposite for the removal of additional pollutants.

2. Materials and Methods

2.1. Chemicals

All used reagents are analytical grade and used without any further purifications. Nitric acid (HNO_3, 64%), sodium hydroxide (NaOH), ferric chloride hexahydrate ($FeCl_3 \cdot 6H_2O$,

98%), and manganese chloride tetrahydrate ($MnCl_2·4H_2O$, 98%) were supplied from Shanghai Chemical Reagent Co. while graphite powder and neutral red (NR), and Lead nitrate $Pb(NO_3)_2$ (99%) were supplied from Sigma-Aldrich, Darmstadt, Germany. We used in all experiments double distilled water.

2.2. Nanocomposite Synthesis

In situ method was used for the synthesis of $MnFe_2O_4$/graphene oxide nanocomposite [41] in which graphene oxide suspension (prepared by dissolving 0.4 g in 200 mL of water) was mixed with manganese chloride tetrahydrate (0.94 g) and ferric chloride hexahydrate (2.54 g), so that the molar ratio of Mn:Fe in the solution is 1:2.7. After that, the mixture's sonication was continued up to half-hour followed by adjustment of mixture pH to 10. Then, a vigorous stirring of the mixture was continued up to one hour at 85 °C. The produced precipitate was finally washed several times and dried. Graphene oxide and $MnFe_2O_4$ NPs were required for characterization and comparison; so synthesized by the Tour method [42] and in situ method [43], respectively.

2.3. Nanocomposite Characterization

The synthesized materials were characterized using different techniques. The materials morphology and size were determined using Transmission Electron Microscopy (TEM, JEOL JEM-1010, JEOL USA, Inc., Massachusetts, USA) as well as Scanning Electron Microscopy (SEM, Zeiss Ultra plus 55, Oberkochen, Germany). The X-ray diffraction (XRD, Bruker D5005, Bruker Co., Massachusetts, USA) was used to determine the crystalline nature and phase purity using monochromatic Cu radiation K_α = 0.15418 nm. Raman spectroscopy was used to study the material structural defects. Fourier transform infrared (FTIR, a Nicolet 6700, Thermo Fisher Scientific, Massachusetts, USA) spectroscopy was used to study the chemical groups in the range of 400 cm^{-1} to 4000 cm^{-1}. X-ray photoelectron spectroscopy (XPS) was used to study the chemical state of the samples. A vibrating sample magnetometer (MicroSense EV9, MicroSense, LLC, Massachusetts, USA) was used to study the sample magnetic properties.

2.4. Batch Adsorption Experiments

In a preliminary test, 8 mg of the synthesized adsorbent was mixed with 50 mL of working solutions of Pb^{2+} and NR in a 100 mL Erlenmeyer flask to determine the optimum conditions of the adsorption. For lead ions (Pb^{2+}) removal, a stock solution was prepared by dissolving (1.6 g) of lead nitrate in distilled water (1000 mL) for all batch experiments at room temperature. The dilution method is used to obtain the desired concentration. To study the pH effect on the adsorption of Pb^{2+} ions over the nanocomposite surface, Pb^{2+} ions solution (50 mg/L, 50 mL) was used to study the adsorption in the pH range (1.0 to 6.0) adjusted using 1 M of NaOH and HNO_3. Also, 50 mg/L of Pb^{2+} ions solution was used to study the contact time effect in the range of 5 to 120 min using 8 mg (adsorbent dosage). 50 mL of 50 mg/L Pb^{2+} ions solutions in the range of 2 to 30 mg were used to study the dosage effect. For neutral red dye, a concentration of (20 mg/L, 6 mL) was used. The pH range was altered as 4 to 9, contact time effect as 30 to 480 min, and dosage effect from 2 to 12 mg. Water bath shaker was used to shake all experiments flasks at 300 rpm. For the analysis of pollutants residues in the solutions after each experiment, the adsorbent was separated using a magnet and the solution was analyzed for the presence of Pb^{2+} ions and NR using atomic adsorption spectroscopy and UV-Vis spectrophotometer at 526 nm, respectively. The synthesized adsorbent adsorption capacity and removal efficiency were calculated according to the following equations:

$$E = [(C_o - C_t)/C_o] \times 100, \tag{1}$$

$$q_e \ (mg/g) = [(C_o - C_t)/m] \times V, \tag{2}$$

where C_t and C_o represent the final and initial pollutant concentration, respectively. m denotes the mass of adsorbent; V denotes the volume of solution. E denotes the removal efficiency and q_e denotes the adsorption capacity (mg/g).

3. Results and Discussions

3.1. Nanocomposite Characterization

The synthesized materials morphology was characterized using a TEM image, as shown in Figure 1. According to Figure 1, the TEM image of $MnFe_2O_4$ nanoparticles in Figure 1a showed an agglomeration of the nanoparticles, while Figure 1b showed stacking of GO sheets that are appeared to be folded and wrinkles. Figure 1c showed the TEM image of $MnFe_2O_4/GO$ nanocomposite that clearly appears the well-distribution of $MnFe_2O_4$ NPs over the GO sheets with nanocomposite size ranging from 11 to 26 nm.
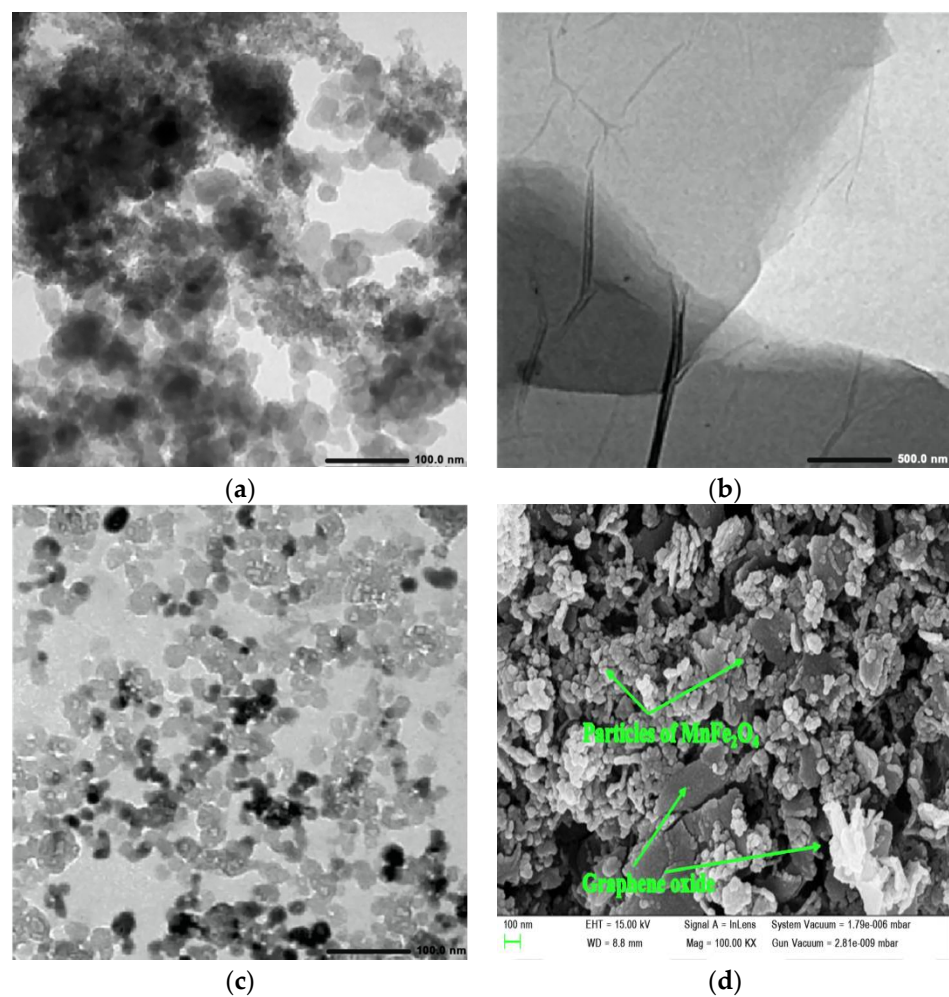
Figure 1. TEM image of $MnFe_2O_4$ nanoparticles (**a**), graphene oxide (**b**), and $MnFe_2O_4$/graphene oxide nanocomposite (**c**); SEM image of $MnFe_2O_4$/graphene oxide nanocomposite (**d**).

Figure 1d showed the SEM image of $MnFe_2O_4/GO$ nanocomposite at high magnification. Figure 1d shows the homogenous distribution of spherical $MnFe_2O_4$ NPs over GO sheets that confirms the TEM image results. $MnFe_2O_4/GO$ nanocomposite XRD was shown in Figure 2a to investigate the crystalline structure and phase purity.
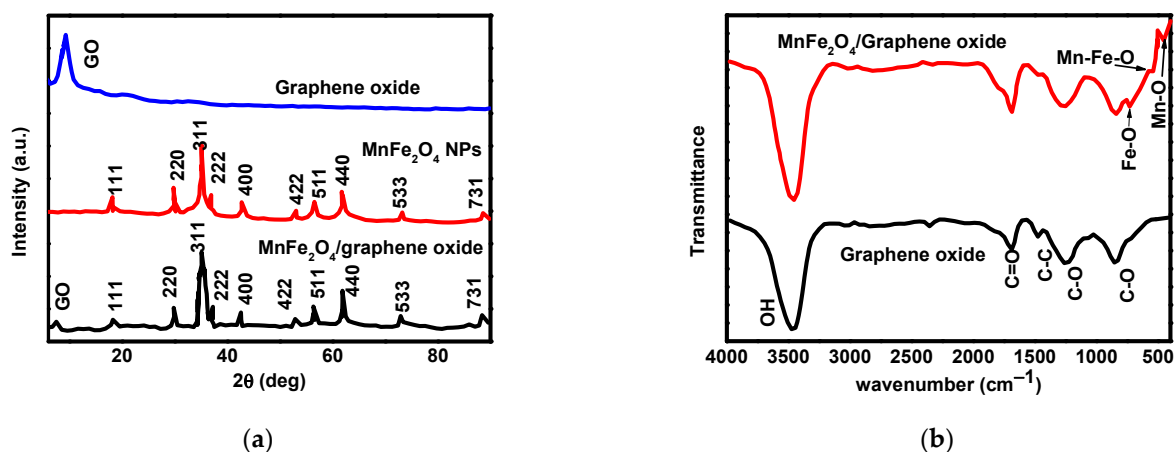
Figure 2. XRD (**a**) and FT-IR (**b**) of MnFe$_2$O$_4$/graphene oxide nanocomposite and its components.

According to Figure 2a, XRD shows the peaks corresponding to (731), (533), (440), (511), (422), (400), (222), (311), and (220) crystal plans that appeared in both XRD of MnFe$_2$O$_4$ and MnFe$_2$O$_4$/graphene oxide nanocomposite. Graphene oxide peak was observed at 12.99° that represents (001) plane. The graphene oxide plane decreased in the XRD of MnFe$_2$O$_4$/graphene oxide nanocomposite, indicating the reduction of graphene oxide during nanocomposite synthesis. The purity of the synthesized sample was indicated from the absence of XRD peaks related to the formation of metal oxides, either manganese or iron, and indicated the formation of the nanocomposite. As nanoparticles grown on graphene oxide surface preclude it from restacking, the peak of graphene oxide is significantly reduced. The average particle size of MnFe$_2$O$_4$ nanoparticles alone and MnFe$_2$O$_4$ in nanocomposite was calculated using the Debye-Scherrer equation, which was found equal to 12 nm and 9 nm, respectively. The decreased size of MnFe$_2$O$_4$ in the nanocomposite was attributed to the blocked growth of nanoparticles from one side during the growth over graphene oxide sheets.

For more details about the nanocomposite composition, FT-IR spectra were shown in Figure 2b to determine the functional groups. According to the FT-IR results, the vibrations of functional groups O-C, C=C, C=O, and OH graphene oxide were represented by 750.20, 1383.48, 1628.34, 1628.34, 1722.43, and 3450 cm^{-1}, respectively [44]. Additionally, MnFe$_2$O$_4$ (Mn-O and Fe-O) bonds are represented by 481.25 and 663.29 cm^{-1}, respectively. The absorption peak at 540 cm^{-1} is a characteristic peak corresponding to the stretching vibrations of the Mn-Fe-O linkage. FT-IR results showed an excellent linkage between graphene oxide and MnFe$_2$O$_4$ NPs [45]. Furthermore, the composition more details were obtained via wide scan XPS, as shown in Figure 3a for MnFe$_2$O$_4$/GO nanocomposite. According to Figure 3a, Fe 2p, Mn 2p, O 1s of adsorbed oxygen, and C 1s in sp2 carbon were represented by peaks at 710.33, 640.14, 528.59, and 284.34, respectively.

The high purity of the synthesized nanocomposite was also indicated by the absence of any other pollutants' peaks in the wide scan XPS.

As one of the advantages of this nanocomposite is the magnetic property that allowing the simple separation using a magnet, we study the magnetization curve of the currently synthesized nanocomposite as shown in Figure 3b. According to Figure 3b, the saturation magnetism (Ms) was 28.8 and 67 emu/g for MnFe$_2$O$_4$/GO and manganese ferrite alone, respectively, indicating the reduced size nanocomposite after the loading of manganese ferrite over graphene oxide. Both of them exhibit superparamagnetic behavior. The nanocomposite's magnetic properties are attributed to the load of magnetic ferrite over the graphene oxide [46,47].

Raman spectra of graphene oxide and MnFe$_2$O$_4$/graphene oxide were showed in Figure 3c. The structural defects are responsible for the D peak that resulted from out of the plane of sp^2 bonded carbon atoms, while the G peak is attributed to in-plane vibrations [48].

The defect of the material was represented by the (ID/IG) intensity ratio. According to Figure 3c, ID/IG ratio for $MnFe_2O_4$/graphene oxide nanocomposite is 1.13 that is higher than that of graphene oxide (which is equal to 0.94), indicating the interaction between graphene oxide's oxygen groups and manganese ferrite nanoparticles [49]. This interaction is responsible for the increased degree of the defect and causes this difference in peak ratio.

(**a**)

(**b**)

(**c**)
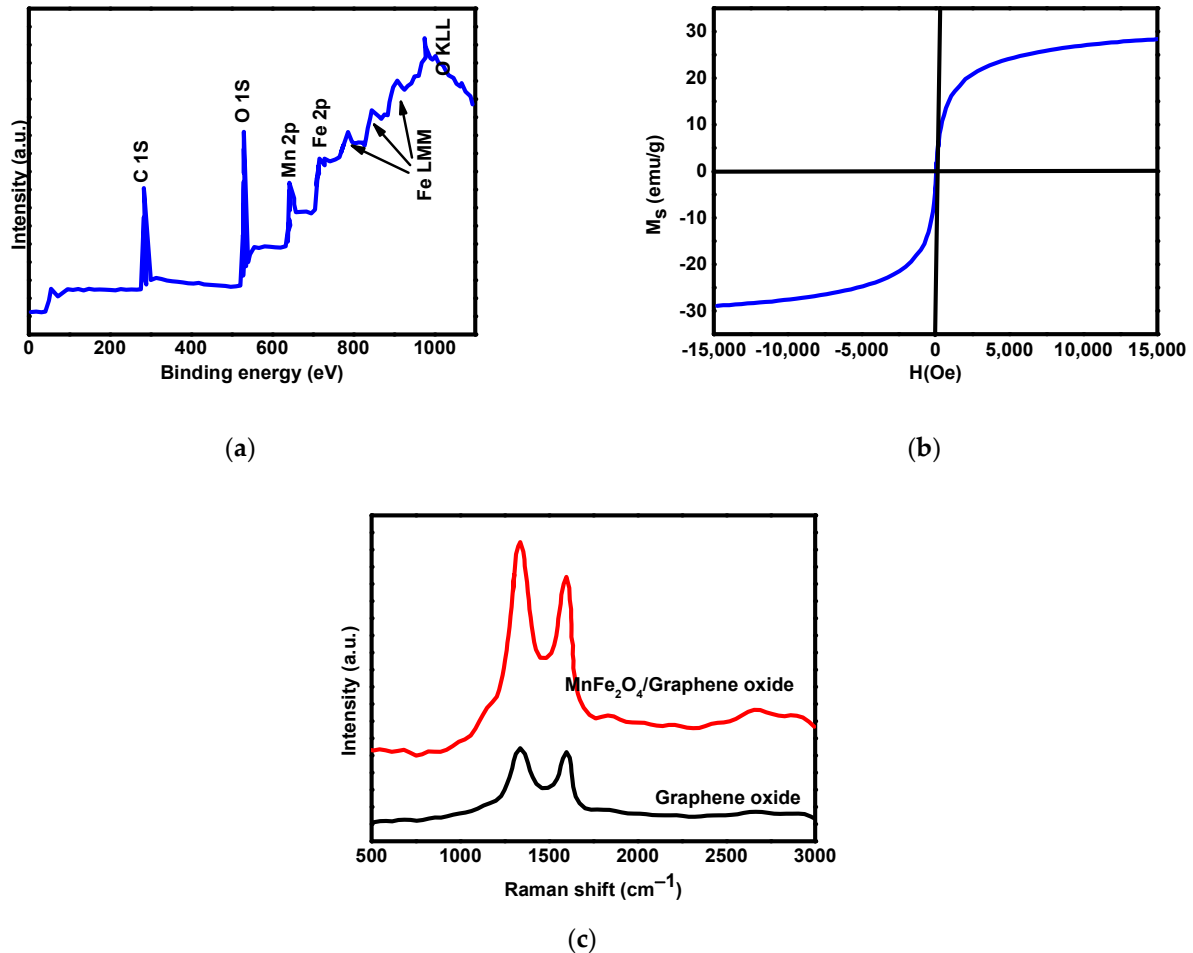
Figure 3. Wide scan XPS (**a**), room temperature magnetization curve (**b**), and Raman spectra (**c**) of $MnFe_2O_4$/GO nanocomposite.

3.2. Effect of Initial Concentration

The ratio between accessible active sites of $MnFe_2O_4$/graphene oxide nanocomposite adsorbent and the concentration of adsorbate (Pb^{2+} and NR dye) is the adsorption efficiency (%) that also associates adsorbent surface coverage. The concentrations range from 10 to 300 and 20 to 200 mg/L were used to study the adsorption of Pb^{2+} and NR over $MnFe_2O_4$/graphene oxide nanocomposite, respectively as shown in Figure 4. According to Figure 4, the increased concentration of the adsorbate led to a decrease of removal efficiency from 99% to 33% for Pb^{2+} ions and from 92.8 to 89% for NR dye. Nevertheless, the increase of concentration led to the increase of adsorption capacity from 63 to 625 mg/g for Pb^{2+} ions and from 20 to 90 mg/g for NR dye due to the accelerated mass transfer of pollutants toward the surface of nanocomposite that attributed to high pollutants concentrations [50]. The removal efficiency reached its maximum value of Pb^{2+} ions and NR adsorption at lower adsorbate concentrations due to high available adsorption active sites. This inverse relationship between adsorption efficiency and adsorption capacity during initial concentration increase was observed in many similar reports.
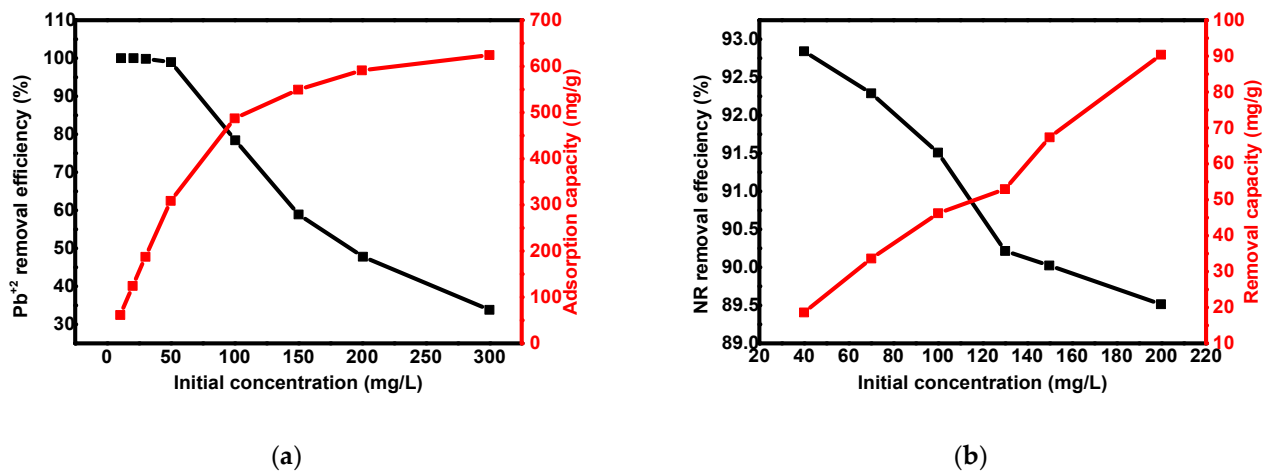
Figure 4. The effect of initial concentration of Pb^{2+} ions (**a**) and neutral red (NR) dye (**b**) for the adsorption over $MnFe_2O_4/GO$ nanocomposite.

3.3. Dose Effect

Adsorption of contaminants dramatically depends on the dose of $MnFe_2O_4/GO$ nanocomposite that extremely affects the removal efficiency of Pb^{2+} ions and NR dye due to the variations in available functional groups responsible for contaminants capturing. The adsorbent dose effect on the adsorption of Pb^{2+} and NR was investigated in dosage range from 2 to 30 mg and 2 to 12 mg, respectively as shown in Figure 5. The volume and concentration of Pb^{2+} ions and NR dye were fixed to be (50 mL, 50 mg/L) and (6 mL, 50 mg/L), respectively. As the amount of nanocomposite dose increased from 2 mg to 8 mg, the removal efficiency of Pb^{2+} ions were increased from 39% to 98.8%. In comparison, the increased dose from 2 mg to 12 mg led to an increase in removal efficiency from 63% to 94%.
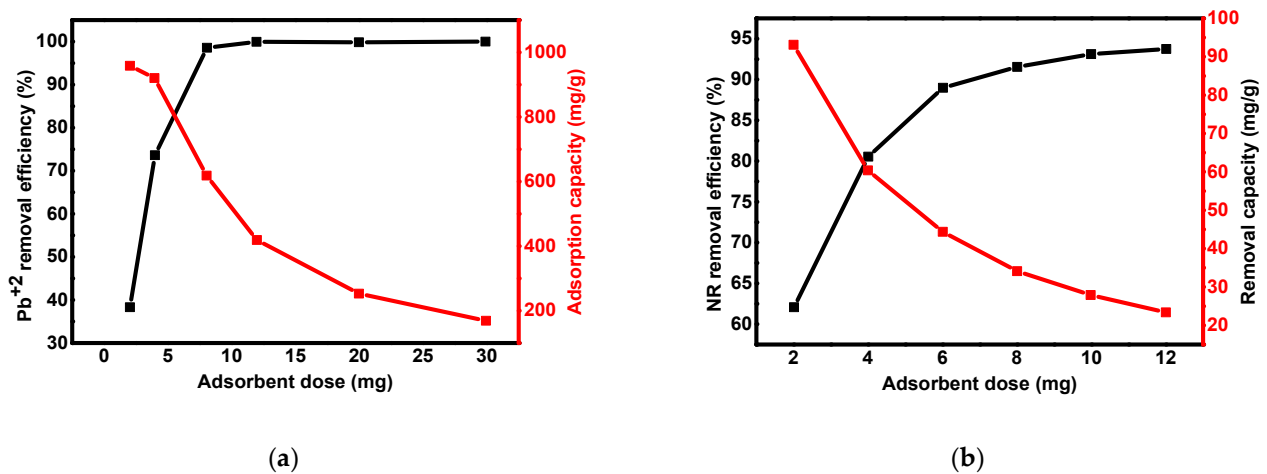
Figure 5. The effect of adsorbent dose on Pb^{2+} ions (**a**) and NR dye (**b**) adsorption over $MnFe_2O_4/GO$ nanocomposite.

The increased overall surface area and the number of active sites accompanying the increased adsorbent dosage are responsible for the nanocomposite's increased adsorption efficiency toward Pb^{2+} and NR dye that easily penetrate these vacant adsorption sites. As observed in Figure 5, the adsorption capacity was decreased by increasing the adsorbent dosage. Pb^{2+} ions and NR dye's absorption capacity were decreased from 960.0 mg/g to 166.0 mg/g and from 80 mg/g to 25 mg/g, respectively with the increase of adsorbent dose. This behavior is due to the high existed number of active adsorption sites compared to the lower number of contaminants molecules that led to lesser adsorbates per unit mass of adsorbent. Thus, the adsorption capacity decreased.

3.4. Effect of pH

The adsorption of Pb^{2+} and NR dye over $MnFe_2O_4$/GO nanocomposite at different pH values were studied, as shown in Figure 6. The studied range was from 2.0 to 6.0 and from 1.5 to 13.0 for Pb^{2+} and NR dye, respectively. According to Figure 6, the removal efficiency for Pb^{2+} ions and NR dye was decreased by the decrease in pH value as predicted. This minimum removal efficiency of Pb^{2+} ions at a low pH value was attributed to the existence of hydronium ions H_3O^+ that compete with the positively charged metal ions on the adsorption sites over adsorbent surfaces [51]. While the increased value of pH enhanced the ionization of carboxylic and hydroxyl groups over the nanocomposite surfaces, increasing the adsorption of metal ions by ionized functional groups [52]. Furthermore, the hydroxides and oxides of lead ions precipitate at a pH of more than 6. The pH increased from 2.0 to 6.0, leading to an increase of Pb^{2+} adsorption capacities over $MnFe_2O_4$/GO nanocomposite from 155.70 to 463.0 mg/g.
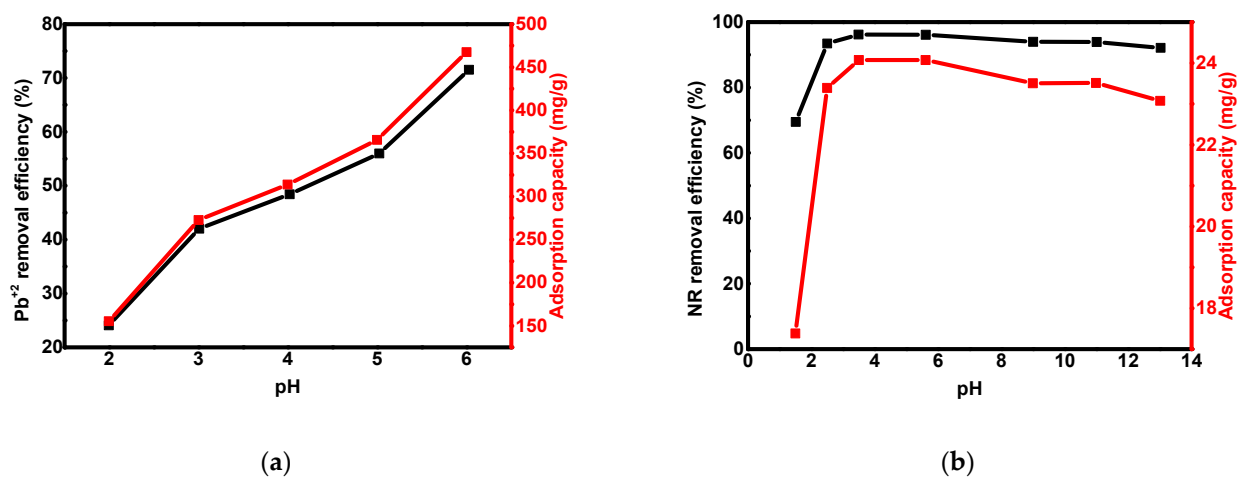

(**a**)   (**b**)

Figure 6. The effect of pH on Pb^{2+} ions (**a**) and NR dye (**b**) adsorption over $MnFe_2O_4$/GO nanocomposite.

Also, for cationic NR dye, at low pH values, the protonation of nanocomposite functional groups and the existing hydronium ions negatively affected the dye adsorption. So, the NR adsorption capacities over $MnFe_2O_4$/GO nanocomposite are increased from 17.0 to 24.0 mg/g by pH increase from 1.5 to 3.5, and the adsorption capacity reached its maximum by pH increase to 6.0 then reached the equilibrium and not affected by the further pH increase. Thus, the optimum pH value for Pb^{2+} and NR dye adsorption over $MnFe_2O_4$/GO nanocomposite was 6.0.

3.5. Effect of Contact Time

One of the most significant factors affecting the adsorption equilibrium is the contact time between adsorbent and pollutant. Pb^{2+} and NR dye's adsorption capacities over $MnFe_2O_4$/GO nanocomposite were investigated at contact time ranging from 0 to 120 min and 0 to 30 min, respectively. The adsorption capacity and removal efficiencies of Pb^{2+} ions and NR dye over $MnFe_2O_4$/GO nanocomposite at different time intervals were shown in Figure 7.

During the contact time effect study, we hold other parameters constant including adsorbent dose, volume, and concentration. The dose, volume, and concentration of Pb^{2+} ions and NR dye were (8 mg, 50 mL, and 50 mg/L) and (12 mg, 6 mL, and 50 mg/L), respectively. According to Figure 7, the removal efficiency and adsorption capacity of Pb^{2+} ions and NR dye increased quickly at the first stage then gradually became slower. The first stage was observed for Pb^{2+} ion and NR dye adsorption at the first 15 and 20 min, respectively. The tremendous available numbers of adsorption sites over $MnFe_2O_4$/GO nanocomposite are responsible for this rapid increase of adsorption capacity at the first

stage. After this stage, the surface saturation was reached, and hence the equilibrium reached with no further significant increase in the adsorption capacity. As indicated from the results, the adsorption equilibrium was not significantly dependent on the adsorbate concentration. The Pb^{2+} ions and NR dye maximum removal were 98% and 94%, respectively. Subsequently, the optimum contact times for Pb^{2+} ions and NR dye were 120 and 30 min, respectively at which the equilibrium reached.
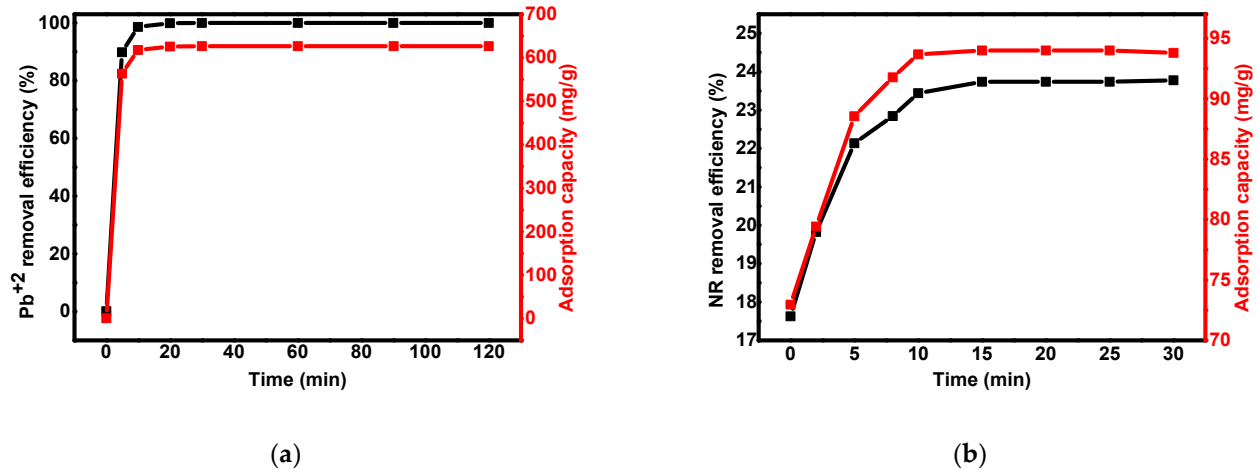

(**a**) (**b**)

Figure 7. The effect of contact time on Pb^{2+} ions (**a**) and NR dye (**b**) adsorption over $MnFe_2O_4$/GO nanocomposite.
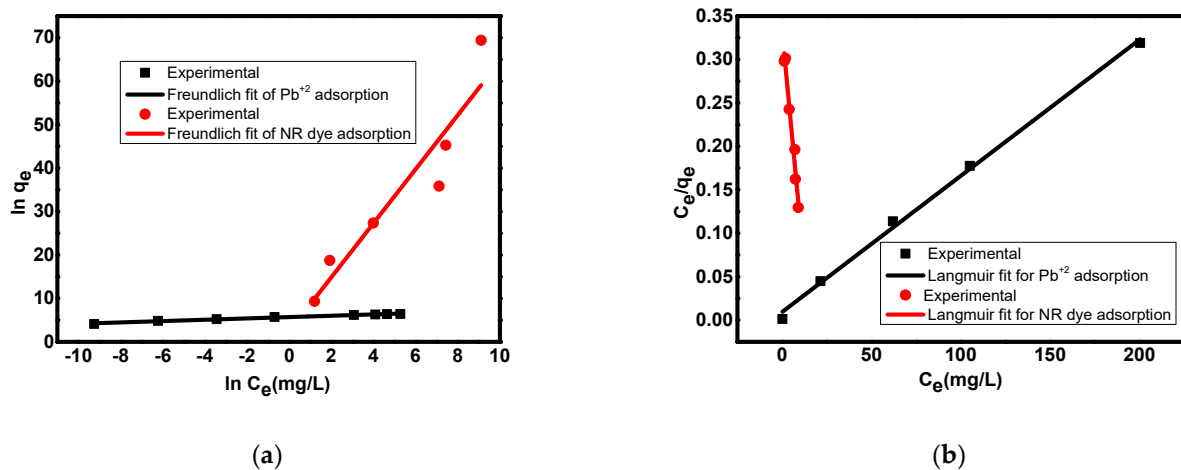
3.6. Adsorption Isotherm

The distribution of the molecule at the equilibrium time between liquid and solid phases is indicated by the adsorption isotherms. The affinities of adsorbent material and insights about surface properties and the understanding of adsorption mechanisms were achieved using both adsorption isotherms. The relation between the adsorption ability of the adsorbent and adsorbate concentration can be completely investigated through adsorption isotherms. The first type of adsorption isotherm is Freundlich isotherm [53] that supposes heterogeneous adsorption and the second is Langmuir isotherm [54] supposes monolayer adsorption with energetically similar active sites. Freundlich isotherm introduces the opinion of heterogeneous surface and multilayer adsorption depending on the fact that non-ideal sorption can be modeled using an exponentially decaying adsorption site energy distribution. The linearized form of the Freundlich model can be written according to the following equation:

$$\ln q_e = \ln K_F + (1/n \ln C_e), \qquad (3)$$

where n and K_F denotes Freundlich constants. C_e and q_e denote equilibrium concentration and adsorption capacity, respectively. The linear fit of $\ln C_e$ against $\ln q_e$ used for these parameters' calculation. More system heterogeneity is indicated by a higher n value. Monolayer chemisorption is represented by the Langmuir isotherm that can be applied according to linearized form according to the following equation:

$$C_e/q_e = (1/K_L q_m) + C_e/q_m, \qquad (4)$$

where K_L, C_e, q_m, and q_e denote Langmuir constant, equilibrium concentration, maximum adsorption capability, and equilibrium adsorption capacity, respectively. The linear fit between C_e and C_e/q_e used for these parameters' calculations. Freundlich and Langmuir adsorption isotherm data are shown in Figure 8 and different parameters were tabulated in Table 1.

Figure 8. Freundlich adsorption isotherm (**a**); Langmuir adsorption isotherm (**b**) for Pb^{2+} and NR dye adsorption over $MnFe_2O_4$/GO nanocomposite.

Table 1. Freundlich and Langmuir adsorption isotherms different parameters for Pb^{2+} ions and NR dye adsorption over $MnFe_2O_4$/GO nanocomposite.

Pollutant	Freundlich			Langmuir		
	K_F	N	R^2	q_m	K_L	R^2
Pb^{2+}	300.0	6.523	0.986	636.94	0.168	0.998
NR dye	11.11	0.160	0.859	46.08	0.065	0.996

According to the results in Table 1, Langmuir isotherm is better fitted to the experimental results for Pb^{2+} ions and NR dye adsorption than Freundlich isotherm. This is indicated from the R^2 value equal to 0.998 and 0.996 (Langmuir fit), 0.986, and 0.859 (Freundlich fit) for Pb^{2+} and NR dye adsorption, respectively.

These results indicate the homogenous energy distribution for active adsorption sites with a monolayer the adsorption process over the adsorbent surface. Langmuir isotherm indicated that Pb^{2+} and NR dye's maximum adsorption capacity are 636.94 and 46.08 mg/g, respectively. Future studies must be including the thermodynamic parameters [55–57] of the adsorption process to get a full image of the removal process.

3.7. Nanocomposite Regeneration

The excellent adsorbent not enough to have excellent adsorption capacity but also must be regenerated according to the industrial, practical, and economic point of view. The adsorbent's reusability ability led to a decrease in the total cost of materials and adsorption processing. For the adsorption/desorption study, the nanocomposite was separated after each adsorption study using a magnet and regenerated again by immersing in 0.2 M HCl to be used again. The nanocomposite $MnFe_2O_4$/GO was studied for reusability toward removing Pb^{2+} ions and NR dye from the water for up to five cycles. The reusability study of $MnFe_2O_4$/GO nanocomposite toward capturing Pb^{2+} ions and NR dye was shown in Figure 9. The results showed that the first cycle has the highest removal efficiency for Pb^{2+} ions and NR dye removal due to the intact pores and active sites. After that, the removal efficiency was slightly decreased due to the damaged sites after the adsorption/desorption cycle. The reusability study indicates that Pb^{2+} ions and NR removals from water are efficient with low cost over the synthesized $MnFe_2O_4$/GO nanocomposite.
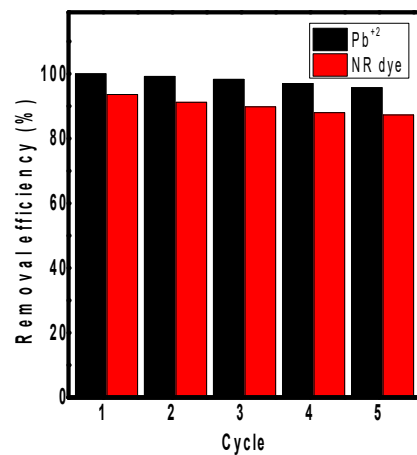
Figure 9. Regeneration of MnFe$_2$O$_4$/GO nanocomposite for Pb^{2+} and NR dye removal up to five cycles.

3.8. Comparative Study

The adsorption capacity of MnFe$_2$O$_4$/GO nanocomposite toward removing Pb^{2+} ions and NR dye from the water was compared with earlier synthesized adsorbents even the same adsorbent synthesized by other methods as shown in Table 2. The information in the table indicates that the nanocomposite synthesized in this study is suitable for removing Pb^{2+} ions and NR dye from water. Also, many reviews reported the application of different materials for the removal of Pb^{2+} ions and dyes [58–60]. According to Table 2, the similar nanocomposite synthesized by Kumar et al. [40] via a different method, conditions, and different percentages of composite phases showed a higher adsorption capacity toward Pb^{2+} ions than that synthesized in the present study. This indicates that MnFe$_2$O$_4$/GO nanocomposite synthesized in the literature has a higher effective surface area and larger functional groups for the chelation of Pb^{2+} ions. However, the most effective adsorbent for Pb2+ removal is few-layered graphene oxide synthesized by Zhao et al. [61]. This high adsorption capacity is attributed to the existence of a large number of oxygen-containing functional groups over its surfaces due to the higher surface site density of few-layered graphene oxide that is about two times more than other graphene materials.

Table 2. Reported adsorbents for adsorption of Pb^{2+} ions and NR dye.

Adsorbent	Pollutant	Isotherm	q_m (mg/g)	Ref.
Banana and orange peels	NR dye	Langmuir	18.0 and 14.0	[62]
Halloysite nanotubes	NR dye	Langmuir	54.85	[63]
Peanut husk	NR dye	Langmuir	37.5	[64]
GO-Fe$_3$O$_4$	NR dye	-	171.3	[47]
GO	Pb^{2+}	Langmuir	488.0	[65]
Carboxylated chitosan magnetic submicron spheres	Pb^{2+}	Langmuir	142.0	[66]
Tetraethylenepentamine modified CS/CoFe$_2$O$_4$	Pb^{2+}	Langmuir	228.0	[67]
GO-EDTA	Pb^{2+}	Langmuir	455.0	[68]
Pinecone activated carbon	Pb^{2+}	Langmuir	27.6	[69]
EDTA-GO	Pb^{2+}	Freundlich	509.0	[70]
GO-MnFe$_2$O$_4$ nanohybrids	Pb^{2+}	Langmuir	673	[40]
Few-layered graphene oxide	Pb^{2+}	Langmuir	842	[61]

4. Conclusions

In this study, $MnFe_2O_4$/GO nanocomposite was synthesized and characterized through the in-situ method for applying water treatment from Pb^{2+} ions and NR dye. Different techniques were used for the nanocomposite characterization, including SEM, TEM, FT-IR, XRD, Raman, and XPS to determine its size, composition, and morphology. The optimal conditions for Pb^{2+} ^{2} and NR dye adsorption over $MnFe_2O_4$/GO nanocomposite were determined by studying different factors, including initial concentration, dose, pH, and contact time. The initial concentration-effect study indicated that the increased concentration of pollutants led to the increase of adsorption capacity from 63 to 625 mg/g and from 20 to 90 mg/g for Pb^{2+} ions and NR dye removal, respectively. The dose-effect study indicated that the increased adsorbent dose led to increased removal efficiency from 39% to 98.8% and from 63% to 94% for Pb^{2+} and NR dye, respectively, due to the increased number of active adsorbent sites. The pH effect study indicated that the optimum pH for both pollutants' adsorption was found to be 6.0. The contact time effect study indicated that Pb^{2+} ions and NR dye's adsorption capacity increased quickly at the first stage and then gradually became slower. The first stage was observed for Pb^{2+} ion and NR dye adsorption at the first 15 and 20 min, respectively. The tremendous available numbers of adsorption sites over $MnFe_2O_4$/GO nanocomposite are responsible for this rapid increase of adsorption capacity at the first stage. After this stage, the surface saturation was reached, and hence the equilibrium reached with no further significant increase in the adsorption capacity. The optimum contact times for Pb^{2+} ions and NR dye were 120 and 30 min, respectively. The monolayer adsorption was concluded for Pb^{2+} and NR dye adsorption over the synthesized nanocomposite that indicated from experimental fitting to Langmuir isotherm. The adsorption capacities are 636.94 and 46.08 mg/g for the adsorption of Pb^{2+} and NR dye, respectively according to Langmuir isotherm. The reusability study of this adsorbent for up to five cycles indicated that this nanocomposite is reusable and stable, reducing the overall cost of treatment. We can conclude that $MnFe_2O_4$/GO nanocomposite is a promising adsorbent for removing Pb^{2+} ions and NR dye from water.

References

1. Tahoon, M.A.; Siddeeg, S.M.; Salem Alsaiari, N.; Mnif, W.; Ben Rebah, F. Effective heavy metals removal from water using nanomaterials: A review. *Processes* **2020**, 8, 645. [CrossRef]
2. Siddeeg, S.M.; Tahoon, M.A.; Rebah, F.B. Agro-industrial waste materials and wastewater as growth media for microbial bioflocculants production: A review. *Mater. Res. Express* **2019**, 7, 012001. [CrossRef]
3. Siddeeg, S.M.; Tahoon, M.A.; Alsaiari, N.S.; Shabbir, M.; Rebah, F.B. Application of Functionalized Nanomaterials as Effective Adsorbents for the Removal of Heavy Metals from Wastewater: A Review. *Curr. Anal. Chem.* **2021**, 17, 4–22. [CrossRef]
4. Jalees, M.I. Synthesis and application of magnetized nanoparticles to remove lead from drinking water: Taguchi design of experiment. *J. Water Sanit. Hyg. Dev.* **2020**, 10, 56–65. [CrossRef]

5.   Batool, A.; Valiyaveettil, S. Chemical transformation of soya waste into stable adsorbent for enhanced removal of methylene blue and neutral red from water. *J. Environ. Chem. Eng.* **2021**, *9*, 104902. [CrossRef]

6.   Mallampati, R.; Valiyaveettil, S. Co-precipitation with calcium carbonate–a fast and nontoxic method for removal of nanopollutants from water? *RSC Adv.* **2015**, *5*, 11023–11028. [CrossRef]

7.   Aitbara, A.; Khelalfa, A.; Bendaia, M.; Abrane, R.; Amrane, A.; Hazourli, S. Treatment of dairy wastewater by electrocoagulation using A-U4G (2017-Al) alloy and pure aluminum as electrode material. *Euro Mediterr. J. Environ. Integr.* **2021**, *6*, 19. [CrossRef]

8.   Xiuyan, L.; Ji, Z.; Hancheng, M.; Fanyi, K.; Cong, T.; Jingang, H.; Chuyan, Y.; Xiangyang, X.; Sheng, T. Degradation of acid orange 7 (AO7) by a bacterium strain Flavobacterium mizutaii L-15. *Water Sci. Technol.* **2020**, *82*, 266–272. [CrossRef]

9.   Hou, J.; Wang, Y.; Zhou, J.; Lu, Y.; Liu, Y.; Lv, X. Photocatalytic degradation of methylene blue using a ZnO/TiO2 heterojunction nanomesh electrode. *Surf. Interfaces* **2021**, *22*, 100889. [CrossRef]

10. Wu, Y.; Gao, Z.; Sun, X.; Cai, H.; Wu, X. Photo-degradation organic dyes by Sb-based organic-inorganic hybrid ferroelectrics. *J. Environ. Sci.* **2021**, *101*, 145–155. [CrossRef] [PubMed]

11. Iqbal, J.; Shah, N.S.; Sayed, M.; Niazi, N.K.; Imran, M.; Khan, J.A.; Khan, Z.U.H.; Hussien, A.G.S.; Polychronopoulou, K.; Howari, F. Nano-zerovalent manganese/biochar composite for the adsorptive and oxidative removal of Congo-red dye from aqueous solutions. *J. Hazard. Mater.* **2021**, *403*, 123854. [CrossRef] [PubMed]

12. Belal, R.M.; Zayed, M.A.; El-Sherif, R.M.; Ghany, N.A.A. Advanced electrochemical degradation of basic yellow 28 textile dye using IrO2/Ti meshed electrode in different supporting electrolytes. *J. Electroanal. Chem.* **2021**, *882*, 114979. [CrossRef]

13. Siddeeg, S.M.; Tahoon, M.A.; Mnif, W.; Ben Rebah, F. Iron oxide/chitosan magnetic nanocomposite immobilized manganese peroxidase for decolorization of textile wastewater. *Processes* **2020**, *8*, 5. [CrossRef]

14. M Siddeeg, S.; A Tahoon, M.; Ben Rebah, F. Simultaneous Removal of Calconcarboxylic Acid, NH4+ and PO43− from Pharmaceutical Effluent Using Iron Oxide-Biochar Nanocomposite Loaded with Pseudomonas putida. *Processes* **2019**, *7*, 800. [CrossRef]

15. Siddeeg, S.M.; Amari, A.; Tahoon, M.A.; Alsaiari, N.S.; Rebah, F.B. Removal of meloxicam, piroxicam and Cd+2 by Fe3O4/SiO2/glycidyl methacrylate-S-SH nanocomposite loaded with laccase. *Alex. Eng. J.* **2020**, *59*, 905–914. [CrossRef]

16. Javadian, H.; Koutenaei, B.B.; Shekarian, E.; Sorkhrodi, F.Z.; Khatti, R.; Toosi, M. Application of functionalized nano HMS type mesoporous silica with N-(2-aminoethyl)-3-aminopropyl methyldimethoxysilane as a suitable adsorbent for removal of Pb (II) from aqueous media and industrial wastewater. *J. Saudi Chem. Soc.* **2017**, *21*, S219–S230. [CrossRef]

17. Amin, M.T.; Alazba, A.A.; Shafiq, M. Comparative Removal of Lead and Nickel Ions onto Nanofibrous Sheet of Activated Polyacrylonitrile in Batch Adsorption and Application of Conventional Kinetic and Isotherm Models. *Membranes* **2021**, *11*, 10. [CrossRef]

18. Silbergeld, E.K. Mechanisms of lead neurotoxicity, or looking beyond the lamppost. *FASEB J.* **1992**, *6*, 3201–3206. [CrossRef] [PubMed]

19. Thabede, P.M.; Shooto, N.D.; Naidoo, E.B. Removal of methylene blue dye and lead ions from aqueous solution using activated carbon from black cumin seeds. *South. Afr. J. Chem. Eng.* **2020**, *33*, 39–50. [CrossRef]

20. Mohammadinezhad, A.; Marandi, G.B.; Farsadrooh, M.; Javadian, H. Synthesis of poly (acrylamide-co-itaconic acid)/MWCNTs superabsorbent hydrogel nanocomposite by ultrasound-assisted technique: Swelling behavior and Pb (II) adsorption capacity. *Ultrason. Sonochemistry* **2018**, *49*, 1–12. [CrossRef] [PubMed]

21. Javadian, H.; Ghasemi, M.; Ruiz, M.; Sastre, A.M.; Asl, S.M.H.; Masomi, M. Fuzzy logic modeling of Pb (II) sorption onto mesoporous NiO/ZnCl2-Rosa Canina-L seeds activated carbon nanocomposite prepared by ultrasound-assisted co-precipitation technique. *Ultrason. Sonochemistry* **2018**, *40*, 748–762. [CrossRef]

22. Javadian, H.; Asadollahpour, S.; Ruiz, M.; Sastre, A.M.; Ghasemi, M.; Asl, S.M.H.; Masomi, M. Using fuzzy inference system to predict Pb (II) removal from aqueous solutions by magnetic Fe3O4/H2SO4-activated Myrtus Communis leaves carbon nanocomposite. *J. Taiwan Inst. Chem. Eng.* **2018**, *91*, 186–199. [CrossRef]

23. Ying, Z.; Chen, X.; Li, H.; Liu, X.; Zhang, C.; Zhang, J.; Yi, G. Efficient Adsorption of Methylene Blue by Porous Biochar Derived from Soybean Dreg Using a One-Pot Synthesis Method. *Molecules* **2021**, *26*, 661. [CrossRef] [PubMed]

24. Sharma, S.; Hasan, A.; Kumar, N.; Pandey, L.M. Removal of methylene blue dye from aqueous solution using immobilized Agrobacterium fabrum biomass along with iron oxide nanoparticles as biosorbent. *Environ. Sci. Pollut. Res.* **2018**, *25*, 21605–21615. [CrossRef]

25. Meng, S.; Yu, S.; Tang, F.; Hu, X.; Lu, J.; Fei, X.; Zhu, M. Fiber engineering of silica-based aerogels with surface specificity and regenerability for continuous removal of dye pollutants from wastewaters. *Microporous Mesoporous Mater.* **2021**, *314*, 110874. [CrossRef]

26. Pelalak, R.; Soltani, R.; Heidari, Z.; Malekshah, R.E.; Aallaei, M.; Marjani, A.; Rezakazemi, M.; Kurniawan, T.A.; Shirazian, S. Molecular dynamics simulation of novel diamino-functionalized hollow mesosilica spheres for adsorption of dyes from synthetic wastewater. *J. Mol. Liq.* **2021**, *322*, 114812. [CrossRef]

27. Çoruh, S.; Geyikçi, F.; Elevli, S. Adsorption of neutral red dye from an aqueous solution onto natural sepiolite using full factorial design. *Clays Clay Miner.* **2011**, *59*, 617–625. [CrossRef]

28. Mashhadi, S.; Javadian, H.; Ghasemi, M.; Saleh, T.A.; Gupta, V.K. Microwave-induced H2SO4 activation of activated carbon derived from rice agricultural wastes for sorption of methylene blue from aqueous solution. *Desalination Water Treat.* **2016**, *57*, 21091–21104.

29. Siddeeg, S.M.; Alsaiari, N.S.; Tahoon, M.A.; Rebah, F.B. The application of nanomaterials as electrode modifiers for the electrochemical detection of ascorbic acid. *Int. J. Electrochem. Sci.* **2020**, *15*, 3327–3346. [CrossRef]

30. Amari, A.; Alalwan, B.; Siddeeg, S.M.; Tahoon, M.A.; Alsaiari, N.S.; Rebah, F.B. Biomolecules Behavior on a Surface of Boron Doped/un-doped Graphene Nanosheets. *Int. J. Electrochem. Sci.* **2020**, *15*, 11427–11436. [CrossRef]

31. Amari, A.; Al Mesfer, M.K.; Alsaiari, N.S.; Danish, M.; Alshahrani, A.M.; Tahoon, M.A.; Rebah, F.B. Electrochemical and Optical Properties of Tellurium Dioxide (TeO2) Nanoparticles. *Int. J. Electrochem. Sci.* **2021**, *16*, 210235. [CrossRef]

32. Amari, A.; Alzahrani, F.M.; Mohammedsaleh Katubi, K.; Alsaiari, N.S.; Tahoon, M.A.; Rebah, F.B. Clay-Polymer Nanocomposites: Preparations and Utilization for Pollutants Removal. *Materials* **2021**, *14*, 1365. [CrossRef]

33. Alsaiari, N.S.; Katubi, K.M.M.; Alzahrani, F.M.; Siddeeg, S.M.; Tahoon, M.A. The Application of Nanomaterials for the Electrochemical Detection of Antibiotics: A Review. *Micromachines* **2021**, *12*, 308. [CrossRef]

34. Liu, J.; Ren, S.; Cao, J.; Tsang, D.C.; Beiyuan, J.; Peng, Y.; Fang, F.; She, J.; Yin, M.; Shen, N. Highly efficient removal of thallium in wastewater by MnFe2O4-biochar composite. *J. Hazard. Mater.* **2021**, *401*, 123311. [CrossRef]

35. Chang, L.; Pu, Y.; Jing, P.; Cui, Y.; Zhang, G.; Xu, S.; Cao, B.; Guo, J.; Chen, F.; Qiao, C. Magnetic core-shell MnFe2O4@ TiO2 nanoparticles decorated on reduced graphene oxide as a novel adsorbent for the removal of ciprofloxacin and Cu (II) from water. *Appl. Surf. Sci.* **2021**, *541*, 148400. [CrossRef]

36. Sadeghfar, F.; Ghaedi, M.; Asfaram, A.; Jannesar, R.; Javadian, H.; Pezeshkpour, V. Polyvinyl alcohol/Fe3O4@ carbon nanotubes nanocomposite: Electrochemical-assisted synthesis, physicochemical characterization, optical properties, cytotoxicity effects and ultrasound-assisted treatment of aqueous based organic compound. *J. Ind. Eng. Chem.* **2018**, *65*, 349–362. [CrossRef]

37. Yu, F.; Chen, J.; Chen, L.; Huai, J.; Gong, W.; Yuan, Z.; Wang, J.; Ma, J. Magnetic carbon nanotubes synthesis by Fenton's reagent method and their potential application for removal of azo dye from aqueous solution. *J. Colloid Interface Sci.* **2012**, *378*, 175–183. [CrossRef] [PubMed]

38. Khan, F.S.A.; Mubarak, N.M.; Tan, Y.H.; Khalid, M.; Karri, R.R.; Walvekar, R.; Abdullah, E.C.; Nizamuddin, S.; Mazari, S.A. A comprehensive review on magnetic carbon nanotubes and carbon nanotube-based buckypaper-heavy metal and dyes removal. *J. Hazard. Mater.* **2021**, *413*, 125375. [CrossRef]

39. Adel, M.; Ahmed, M.A.; Mohamed, A.A. A facile and rapid removal of cationic dyes using hierarchically porous reduced graphene oxide decorated with manganese ferrite. *FlatChem* **2021**, *26*, 100233. [CrossRef]

40. Kumar, S.; Nair, R.R.; Pillai, P.B.; Gupta, S.N.; Iyengar, M.; Sood, A. Graphene oxide–MnFe2O4 magnetic nanohybrids for efficient removal of lead and arsenic from water. *ACS Appl. Mater. Interfaces* **2014**, *6*, 17426–17436. [CrossRef] [PubMed]

41. Hieu, N.H. Removal of Cd (II) from water by using graphene oxide–MnFe2O4 magnetic nanohybrids. *Vietnam J. Sci. Technol.* **2017**, *55*, 109. [CrossRef]

42. Marcano, D.C.; Kosynkin, D.V.; Berlin, J.M.; Sinitskii, A.; Sun, Z.; Slesarev, A.; Alemany, L.B.; Lu, W.; Tour, J.M. Improved synthesis of graphene oxide. *ACS Nano* **2010**, *4*, 4806–4814. [CrossRef]

43. Ma, Z.; Zhao, D.; Chang, Y.; Xing, S.; Wu, Y.; Gao, Y. Synthesis of MnFe 2 O 4@ Mn–Co oxide core–shell nanoparticles and their excellent performance for heavy metal removal. *Dalton Trans.* **2013**, *42*, 14261–14267. [CrossRef]

44. Cui, H.-J.; Shi, J.-W.; Yuan, B.; Fu, M.-L. Synthesis of porous magnetic ferrite nanowires containing Mn and their application in water treatment. *J. Mater. Chem. A* **2013**, *1*, 5902–5907. [CrossRef]

45. Yang, Y.; Shi, H.; Wang, Y.; Shi, B.; Guo, L.; Wu, D.; Yang, S.; Wu, H. Graphene oxide/manganese ferrite nanohybrids for magnetic resonance imaging, photothermal therapy and drug delivery. *J. Biomater. Appl.* **2016**, *30*, 810–822. [CrossRef] [PubMed]

46. Zhao, G.; Li, J.; Ren, X.; Chen, C.; Wang, X. Few-layered graphene oxide nanosheets as superior sorbents for heavy metal ion pollution management. *Environ. Sci. Technol.* **2011**, *45*, 10454–10462. [CrossRef] [PubMed]

47. Xie, G.; Xi, P.; Liu, H.; Chen, F.; Huang, L.; Shi, Y.; Hou, F.; Zeng, Z.; Shao, C.; Wang, J. A facile chemical method to produce superparamagnetic graphene oxide–Fe 3 O 4 hybrid composite and its application in the removal of dyes from aqueous solution. *J. Mater. Chem.* **2012**, *22*, 1033–1039. [CrossRef]

48. Trinh, T.T.P.N.X.; Quang, D.T.; Tu, T.H.; Dat, N.M.; Linh, V.N.P.; Loan, T.T.; Hang, P.T.; Phuong, N.T.L.; Phong, M.T.; Nam, H.M. Fabrication, characterization, and adsorption capacity for cadmium ions of graphene aerogels. *Synth. Met.* **2019**, *247*, 116–123. [CrossRef]

49. Minh Dat, N.; Linh, V.N.P.; Huy, L.A.; Huong, N.T.; Tu, T.H.; Phuong, N.T.L.; Nam, H.M.; Thanh Phong, M.; Hieu, N.H. Fabrication and antibacterial activity against Pseudomonas aeruginosa and Staphylococcus aureus of silver nanoparticle decorated reduced graphene oxide nanocomposites. *Mater. Technol.* **2019**, *34*, 369–375. [CrossRef]

50. Hor, K.Y.; Chee, J.M.C.; Chong, M.N.; Jin, B.; Saint, C.; Poh, P.E.; Aryal, R. Evaluation of physicochemical methods in enhancing the adsorption performance of natural zeolite as low-cost adsorbent of methylene blue dye from wastewater. *J. Clean. Prod.* **2016**, *118*, 197–209. [CrossRef]

51. Singh, S.; Kapoor, D.; Khasnabis, S.; Singh, J.; Ramamurthy, P.C. Mechanism and kinetics of adsorption and removal of heavy metals from wastewater using nanomaterials. *Environ. Chem. Lett.* **2021**, 1–31. [CrossRef]

52. Ghobadi, M.; Gharabaghi, M.; Abdollahi, H.; Boroumand, Z.; Moradian, M. MnFe2O4-graphene oxide magnetic nanoparticles as a high-performance adsorbent for rare earth elements: Synthesis, isotherms, kinetics, thermodynamics and desorption. *J. Hazard. Mater.* **2018**, *351*, 308–316. [CrossRef] [PubMed]

53. Freundlich, H. Over the adsorption in solution. *J. Phys. Chem* **1906**, *57*, 1100–1107.

54. Langmuir, I. The adsorption of gases on plane surfaces of glass, mica and platinum. *J. Am. Chem. Soc.* **1918**, *40*, 1361–1403. [CrossRef]

55. Gomaa, E.A.; Tahoon, M.A.; Negm, A. Aqueous micro-solvation of Li+ ions: Thermodynamics and energetic studies of Li +-(H2O) n (n = 1–6) structures. *J. Mol. Liq.* **2017**, *241*, 595–602. [CrossRef]

56. Gomaa, E.A.; Tahoon, M.A. Ion association and solvation behavior of copper sulfate in binary aqueous–methanol mixtures at different temperatures. *J. Mol. Liq.* **2016**, *214*, 19–23. [CrossRef]

57. Tahoon, M.; Gomaa, E.; Suleiman, M. Aqueous Micro-hydration of Na + (H2O) n = 1-7 Clusters: DFT Study. *Open Chem.* **2019**, *17*, 260–269.

58. Thakur, K.; Kandasubramanian, B. Graphene and graphene oxide-based composites for removal of organic pollutants: A review. *J. Chem. Eng. Data* **2019**, *64*, 833–867. [CrossRef]

59. Bhatia, M.; Babu, R.S.; Sonawane, S.; Gogate, P.; Girdhar, A.; Reddy, E.; Pola, M. Application of nanoadsorbents for removal of lead from water. *Int. J. Environ. Sci. Technol.* **2017**, *14*, 1135–1154. [CrossRef]

60. Bharti, M.K.; Gupta, S.; Chalia, S.; Garg, I.; Thakur, P.; Thakur, A. Potential of Magnetic Nanoferrites in Removal of Heavy Metals from Contaminated Water: Mini Review. *J. Supercond. Nov. Magn.* **2020**, *33*, 3651–3665. [CrossRef]

61. Zhao, G.; Ren, X.; Gao, X.; Tan, X.; Li, J.; Chen, C.; Huang, Y.; Wang, X. Removal of Pb (II) ions from aqueous solutions on few-layered graphene oxide nanosheets. *Dalton Trans.* **2011**, *40*, 10945–10952. [CrossRef] [PubMed]

62. Annadurai, G.; Juang, R.-S.; Lee, D.-J. Use of cellulose-based wastes for adsorption of dyes from aqueous solutions. *J. Hazard. Mater.* **2002**, *92*, 263–274. [CrossRef]

63. Luo, P.; Zhao, Y.; Zhang, B.; Liu, J.; Yang, Y.; Liu, J. Study on the adsorption of Neutral Red from aqueous solution onto halloysite nanotubes. *Water Res.* **2010**, *44*, 1489–1497. [CrossRef] [PubMed]

64. Runping, H.; Pan, H.; Zhaohui, C.; Zhenhui, Z.; Mingsheng, T. Kinetics and isotherms of neutral red adsorption on peanut husk. *J. Environ. Sci.* **2008**, *20*, 1035–1041.

65. Madadrang, C.J.; Kim, H.Y.; Gao, G.; Wang, N.; Zhu, J.; Feng, H.; Gorring, M.; Kasner, M.L.; Hou, S. Adsorption behavior of EDTA-graphene oxide for Pb (II) removal. *ACS Appl. Mater. Interfaces* **2012**, *4*, 1186–1193. [CrossRef]

66. Xu, Y.; Dang, Q.; Liu, C.; Yan, J.; Fan, B.; Cai, J.; Li, J. Preparation and characterization of carboxyl-functionalized chitosan magnetic microspheres and submicrospheres for Pb2+ removal. *Colloids Surf. A Physicochem. Eng. Asp.* **2015**, *482*, 353–364. [CrossRef]

67. Fan, C.; Li, K.; Li, J.; Ying, D.; Wang, Y.; Jia, J. Comparative and competitive adsorption of Pb (II) and Cu (II) using tetraethylene-pentamine modified chitosan/CoFe2O4 particles. *J. Hazard. Mater.* **2017**, *326*, 211–220. [CrossRef] [PubMed]

68. Carpio, I.E.M.; Mangadlao, J.D.; Nguyen, H.N.; Advincula, R.C.; Rodrigues, D.F. Graphene oxide functionalized with ethylenedi-amine triacetic acid for heavy metal adsorption and anti-microbial applications. *Carbon* **2014**, *77*, 289–301. [CrossRef]

69. Momčilović, M.; Purenović, M.; Bojić, A.; Zarubica, A.; Ranđelović, M. Removal of lead (II) ions from aqueous solutions by adsorption onto pine cone activated carbon. *Desalination* **2011**, *276*, 53–59. [CrossRef]

70. Cui, L.; Wang, Y.; Gao, L.; Hu, L.; Yan, L.; Wei, Q.; Du, B. EDTA functionalized magnetic graphene oxide for removal of Pb (II), Hg (II) and Cu (II) in water treatment: Adsorption mechanism and separation property. *Chem. Eng. J.* **2015**, *281*, 1–10. [CrossRef]